PAPER • OPEN ACCESS

A study of beam ion and deuterium–deuterium fusion-born triton transports due to energetic particle-driven magnetohydrodynamic instability in the large helical device deuterium plasmas

To cite this article: K. Ogawa *et al* 2021 *Nucl. Fusion* **61** 096035

OPEN ACCESS
IOP Publishing | International Atomic Energy Agency Nuclear Fusion
Nucl. Fusion **61** (2021) 096035 (10pp) https://doi.org/10.1088/1741-4326/ac0d8a

A study of beam ion and deuterium–deuterium fusion-born triton transports due to energetic particle-driven magnetohydrodynamic instability in the large helical device deuterium plasmas

K. Ogawa[1,2,*], M. Isobe[1,2], H. Nuga[1], S. Kamio[1], Y. Fujiwara[1], M.I. Kobayashi[1,2], S. Sangaroon[1,3], E. Takada[4], R. Seki[1,2], H. Yamaguchi[1,2], S. Murakami[5], J. Jo[6] and M. Osakabe[1,2]

[1] National Institute for Fusion Science, National Institutes of Natural Sciences, Toki, Japan
[2] The Graduate University for Advanced Studies, SOKENDAI, Toki, Japan
[3] Mahasarakham University, Maha Sarakham, Thailand
[4] National Institute of Technology, Toyama College, Toyama, Japan
[5] Kyoto University, Kyoto, Japan
[6] Korea Institute of Fusion Science, Daejeon, Republic of Korea

E-mail: ogawa.kunihiro@nifs.ac.jp

Received 19 April 2021, revised 2 June 2021
Accepted for publication 22 June 2021
Published 17 August 2021

Abstract

Understanding energetic particle transport due to magnetohydrodynamic instabilities excited by energetic particles is essential to apprehend alpha particle confinement in a fusion burning plasma. In the large helical device (LHD), beam ion and deuterium–deuterium fusion-born triton transport due to resistive interchange mode destabilized by helically-trapped energetic ions (EIC) are studied employing comprehensive neutron diagnostics, such as the neutron flux monitor and a newly developed scintillating fiber detector characterized by high detection efficiency. Beam ion transport due to EIC is studied in deuterium plasmas with full deuterium or hydrogen/deuterium beam injections. The total neutron emission rate (S_n) measurement indicates that EIC induces about a 6% loss of passing transit beam ions and a 60% loss of helically-trapped ions. The loss rate of helically-trapped ions, which drive EIC, is larger than the loss rate of passing transit beam ions. Furthermore, the drop of S_n increasing linearly with the EIC amplitude shows that barely confined beam ions existing near the confinement-loss boundary are lost due to EIC. In full deuterium conditions, a study of deuterium–deuterium fusion-born triton transport due to EIC is performed by time-resolved measurement of total secondary deuterium–tritium neutron emission rate (S_{n_DT}). Drop of S_{n_DT} increases

*Author to whom any correspondence should be addressed.

substantially with EIC amplitude to the third power and reaches up to 30%. The relation shows that not only tritons confined in confined-loss boundary, but also tritons confined in the inner region of a plasma, are substantially transported.

Keywords: large helical device, energetic particle confinement, magnetohydrodynamic instability, neutron diagnostics

(Some figures may appear in colour only in the online journal)

1. Introduction

One of the primary topics for realizing a fusion reactor is the confinement of deuterium–tritium (DT) fusion-born alpha particles, which are the primary heating source in a fusion burning plasma. The sustainment of a fusion burning plasma becomes feasible with the satisfactory confinement of alpha particles. In particular, alpha particle transport due to magnetohydrodynamic (MHD) instability excited by the alpha particle pressure is one of the topics gathering attention [1]. In the DT experiments performed in TFTR, it was reported that the kink and the ballooning MHD instabilities induced an increase in alpha particle losses and a decrease in DT neutron emission rate [2]. In these experiments, no alpha particle loss due to alpha-particle-excited MHD instabilities was observed. The reason was that the amplitude of MHD instabilities in DT discharges was much smaller than the amplitude of MHD instabilities excited in the neutral beam (NB) heated or ion cyclotron heated deuterium discharges. In JET, excitation of alpha-particle-driven MHD instabilities and transport of alpha particles was tried in the DTE1 campaign. However, the alpha-particle-driven MHD instability remained in the stable region [3]. Currently, JET teams are preparing the scenarios in order to observe alpha-particle-driven MHD instability [4]. Therefore, the self-consistent study of non-linear alpha particle transport due to an alpha-particle-driven MHD instability is difficult in currently conducted fusion plasma experiments.

Instead of DT-born energetic alpha particle transport study, studies of energetic particle transport using NB ions, ion cyclotron heated tail ions, and fusion products have been intensively studied in existing fusion devices. In tokamaks, studies of energetic particle transport due to energetic-particle-driven MHD instabilities have been performed using neutral beam injection and ion cyclotron heating [5]. In deuterium plasmas, following deuterium–deuterium (DD) reactions D + D -> ^{3}He (0.8 MeV) + n (2.5 MeV) and D + D -> T (1.0 MeV) + p (3.0 MeV) occurs. In addition, if DD fusion-born 1 MeV tritons are sufficiently confined to slow down, a secondary DT reaction D + T -> ^{4}He (3.5 MeV) + n (14 MeV) arises. Neutron diagnostics play an important role in progressing energetic particle confinement studies, because neutrons are mainly created by the fusion reaction between an energetic particle and a bulk plasma in currently performed plasma experiments using energetic particle heating [6]. In deuterium experiments in DIII-D and ASDEX Upgrade, time-resolved neutron flux measurement using plastic scintillation detectors showed the degradation of global beam ion confinement by a fishbone instability [7, 8]. The radial transport of energetic particles caused by an energetic particle mode in deuterium discharge in JT-60U [9] and the radial transport of energetic particles due to a fishbone in deuterium–tritium discharge in TFTR [10] were observed by neutron profile measurement. In addition, in DIII-D, secondary deuterium–tritium and deuterium–helium3 burnup degraded from the theoretical calculation due to sawtooth activity [11]. The change of secondary DT neutron emission profile showed that no more than 10% of tritons at the axis were redistributed due to sawtooth in JET [12]. Tritons existing in the peripheral region were transported due to the toroidal Alfvén eigenmode in JT-60U [13].

In stellarator/helical devices, which have an advantage in steady-state operation, energetic particle confinement study has been led by the large helical device (LHD) [14]. In hydrogen experiments, radial transport [15, 16] and beam ion loss [17] due to the Alfvén eigenmode [18] have been studied. In these studies, the loss process of the energetic ion due to the Alfvén eigenmode was discussed based on the relation between loss flux and the amplitude of the Alfvén eigenmode [19]. Based on the theoretical/numerical simulation of energetic ion loss this shows that the relation becomes linear when the dominant loss process is convective, and the relation becomes quadratic when the dominant loss process is diffusive [20]. The relation with higher exponentiation will appear due to strong transport [21]. A study of energetic ion loss due to the toroidal Alfvén eigenmode showed that the dominant loss process changed according to the plasma center position due to the change of energetic ion orbit and eigenfunction of the toroidal Alfvén eigenmode [22]. Comparing experimental results and the numerical simulation results revealed the loss process of beam ions due to the Alfvén eigenmode [23, 24].

The study is significantly advancing in the deuterium experiment initiated in March 2017 in the LHD [25–29]. In the deuterium experiment of the LHD, an energetic particle behavior has been mainly studied using NB ions and DD fusion-born tritons [30]. A study of confinement of short-pulsed beam ions showed that the behavior of short-pulsed beam ions in MHD quiescent plasmas could be described as the neoclassical theory. Moreover, DD fusion-born triton confinement capability is comparable with tokamaks having a similar minor radius [31]. Although it was stated that stellarators and helical devices are unfavorable in energetic particle confinement compared with

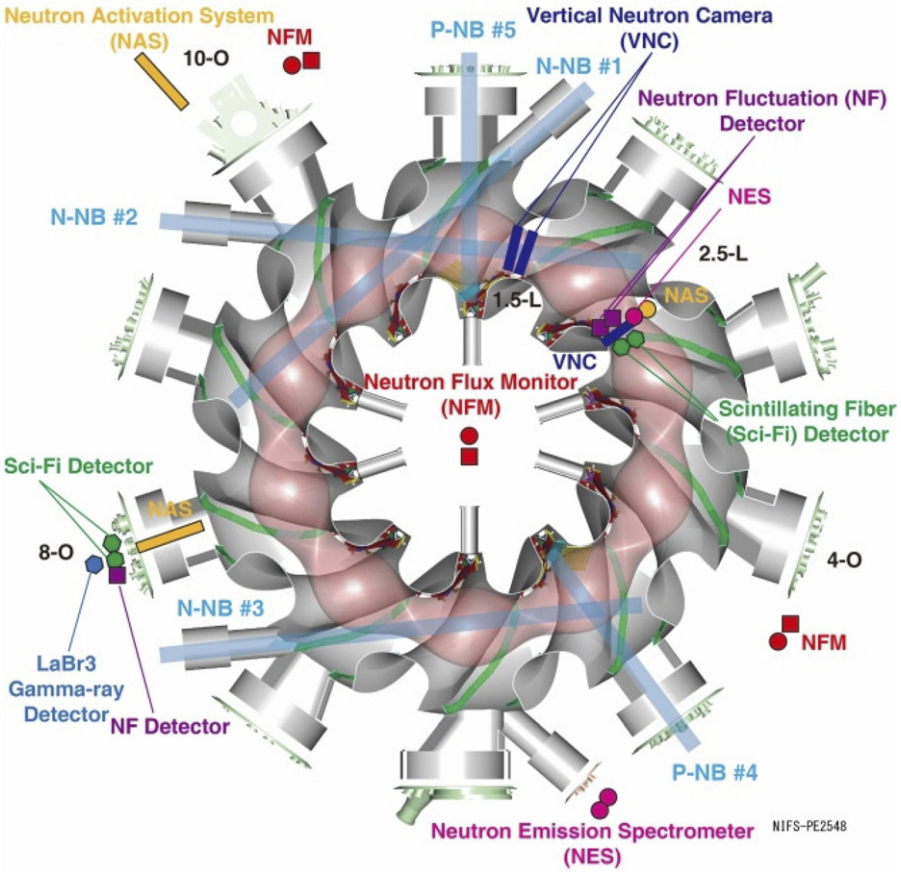

Figure 1. Arrangement of neutral beam injectors and comprehensive neutron diagnostics in the LHD.

tokamaks, these results indicated that stellarators and helical devices have a similar performance in an energetic confinement ability in MHD quiescent plasmas. In the previous MHD instability-induced energetic particle transport study, the radial transport of helically-trapped beam ions due to energetic-ion-driven resistive interchange mode (EIC) has been studied using vertical neutron cameras [32–34]. The experiment and numerical simulation showed that EIC significantly affects the confinement of helically-trapped beam ions, which are the driving source of EIC [35–37]. However, the effects of EIC on passing transit beam ions, which are the primary heating source of LHD, and DD fusion-born tritons are still unknown. In this paper, research on the transport of beam ions and DD fusion-born tritons due to energetic-ion-driven MHD instabilities using the neutron flux monitor and a scintillating-fiber (Sci-Fi) detector is reported in order to contribute to our understanding of energetic ion transport due to MHD instabilities in a fusion burning plasma.

2. Experimental setups

2.1. Neutral beam injector and comprehensive neutron diagnostics in the LHD

Studies of energetic particle confinement due to energetic-ion-driven MHD instability have been performed using intensive NB injectors and comprehensive neutron diagnostics in the LHD [37]. Figure 1 shows the arrangement of NB injectors and comprehensive neutron diagnostics. The LHD is equipped with three tangential NB injectors (N-NB #1-#3) and two perpendicular NB injectors (P-NB #4-#5). Each tangential NB injector has two negative-ion-based sources whose acceleration energy reaches 180 keV. The injection power of an N-NB reaches 3 MW for a deuterium beam injection and reaches 6 MW for a hydrogen beam injection. Each perpendicular NB injector has four positive-ion-based sources whose acceleration energy reaches 60/80 keV. The injection power of a P-NB reaches 10 MW for a deuterium beam injection. These NBs can produce a steep gradient of energetic ions, which could be a driving source of energetic-ion-driven MHD instabilities such as the toroidal Alfvén eigenmode [38], energetic-ion-driven geodesic acoustic mode [39, 40], and EIC classified into energetic particle mode [41, 42]. In deuterium experiments started from March 2017 in the LHD, comprehensive neutron diagnostics have been employed to expand energetic ion confinement research. The neutron flux monitor (NFM), composed of three sets of thermal neutron detectors [43, 44], is utilized to measure the total neutron emission rate (S_n), which reflects the global confinement of deuterium beam ions because neutrons are mainly created by beam deuteron and plasma deuteron reactions. The NFM covers six orders of magnitudes and implements time-resolved measurement within 0.5 ms resolution. A Sci-Fi detector measures the time evolution of the DT neutron emission rate (S_{n_DT}). A Sci-Fi detector is many

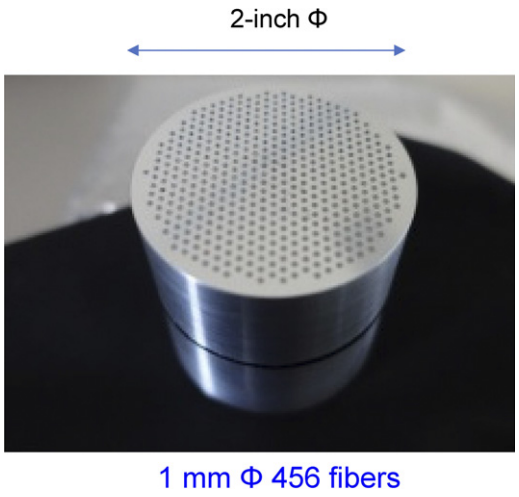

Figure 2. A detector head of middle Sci-Fi detector utilized to measure DT neutron emission rate. 456 Sci-Fis having 1 mm diameter are embedded into the aluminum substrate.

Sci-Fis embedded into an aluminum substrate coupled with a photomultiplier tube (H7195, Hamamatsu K. K.). A large pulse caused by a DT neutron is discriminated from the smaller pulse, which is mainly created by low-energy neutrons and gamma-rays, by pulse height discrimination. A Sci-Fi detector was originated in the Los Alamos National Laboratory and applied in TFTR [45] and JT-60U [13]. Based on the original design of the Sci-Fi detector, we developed several types of Sci-Fi detectors having different detection efficiency to DT neutrons [31, 46–49]. In this study, the Sci-Fi detector having 456 Sci-Fis, namely the middle Sci-Fi detector, is used to measure $S_{\mathrm{n\_DT}}$ with the fine time resolution (figure 2). The length and the diameter of Sci-Fi are 5 cm and 1 mm, respectively. The Sci-Fi detector signal is directly fed into the data acquisition system consisting of the pulse height discriminator and the time history of pulse counts (APV2500C, Techno AP Co. Ltd.). The discrimination level of the pulse height for extracting the DT neutron-induced signal is set to be −71 mV with the high voltage of the photomultiplier tube (H7194, Hamamatsu K. K.) with 1100 V. The size of the time-bin is set to be 1 ms. Note that the Sci-Fi detector is absolutely calibrated by the neutron activation system [28, 50] using silicon foils to evaluate $S_{\mathrm{n\_DT}}$ from the pulse counting rate of the Sci-Fi detector.

2.2. Typical energetic particle orbit in the LHD

In the LHD, twin twisted coils mainly produce the magnetic field for plasma confinement. Therefore, three types of orbits, e.g. co-going transit, counter-going transit, and helically trapped, exist. Tangential N-NBs mainly produce passing transit beam ions, whereas perpendicular P-NBs mainly produce helically-trapped beam ions. A collisionless Larmor orbit calculation based on the magnetic field in the vacuum without including plasma MHD equilibrium using the Lorentz orbit code (LORBIT) [51] is performed to compare beam ion and DD-born 1 MeV orbits at the toroidal magnetic field strength B_{t} of 2.75 T and the magnetic axis position in vacuum R_{ax} of 3.60 m. Figures 3(*a*) and (*b*) show the Poincaré plot of typical passing transit and helically-trapped beam ions at the vertically elongated poloidal cross-section. Here, the color contour shows the magnetic field strength and the black line shows the magnetic flux surface. The start point of orbits is set to be R of 3.70 m and Z of −0.50 m at this toroidal angle. The orbit following time is set to be 2×10^{-4} s. Here, the energy/pitch angle of co-going transit, counter-going transit, and helically-trapped beam ions are set to be 180 keV/30 degrees, 180 keV/150 degrees, and 80 keV/91 degrees, respectively. These energies and the pitch angles are typical values of NB ions in LHD [22]. Passing transit beam ions almost align with the magnetic flux surface, whereas the helically-trapped beam ion has a poloidal structure because a helically-trapped beam ion stays at the weak magnetic field region called a helical ripple valley [52]. Figures 3(*c*) and (*d*) show the Poincaré plot of typical passing transit and helically-trapped 1 MeV tritons at the vertically elongated poloidal cross-section. Here, the start position and the pitch angle of tritons are set to be the same as the start position and the pitch angle of beam ions shown in figures 3(*a*) and (*b*) for comparison. The Larmor radius of 1 MeV tritons corresponding to the thickness of the Poincaré plot is larger than the Larmor radius of beam ions. The Larmor radius evaluated by the energy is ∼9 cm, which is approximately three times larger than a 180 keV deuteron and is equivalent to ∼15% of the averaged minor radius of a plasma. The orbit substantially deviates from the flux surface for passing transit tritons. In particular, a co-going transit triton has a re-entering orbit which crosses the last closed flux surface and returns to the plasma confined region. Although the re-entering orbit crosses the last closed flux surface at the outboard side of the torus, the orbit passes through the normalized minor radius of ∼0.2 at the inboard side. For a helically-trapped beam ion, the orbit largely deviates from the helical ripple valley due to the large Larmor radius. The Poincaré plot suggests that 1 MeV tritons are barely confined in the LHD. Also, there is a so-called transition orbit that exists in the boundary of passing-transit and helically-trapped orbits where the pitch angle is approximately 60 degrees. The transition orbit is unstable and shows inadequate confinement [53]. The passing-transit and helically-trapped ions existing near the transition region can be relatively easily lost because of small momentum changes due to the collision or MHD instability.

3. Energetic ion transport due to energetic ion driven resistive interchangemode

3.1. Beam ion transport due to EIC

Experiments were performed in relatively low-density deuterium plasma conditions with intense P-NB injections to excite EIC (figure 4). A plasma was initiated with the electron cyclotron heating and then deuterium beams were injected using three N-NBs and two P-NBs. The total deposition power of the N-NBs reached 6 MW and the total injection power of the P-NBs reached 17 MW. The central electron temperature measured by Thomson scattering diagnostics and the

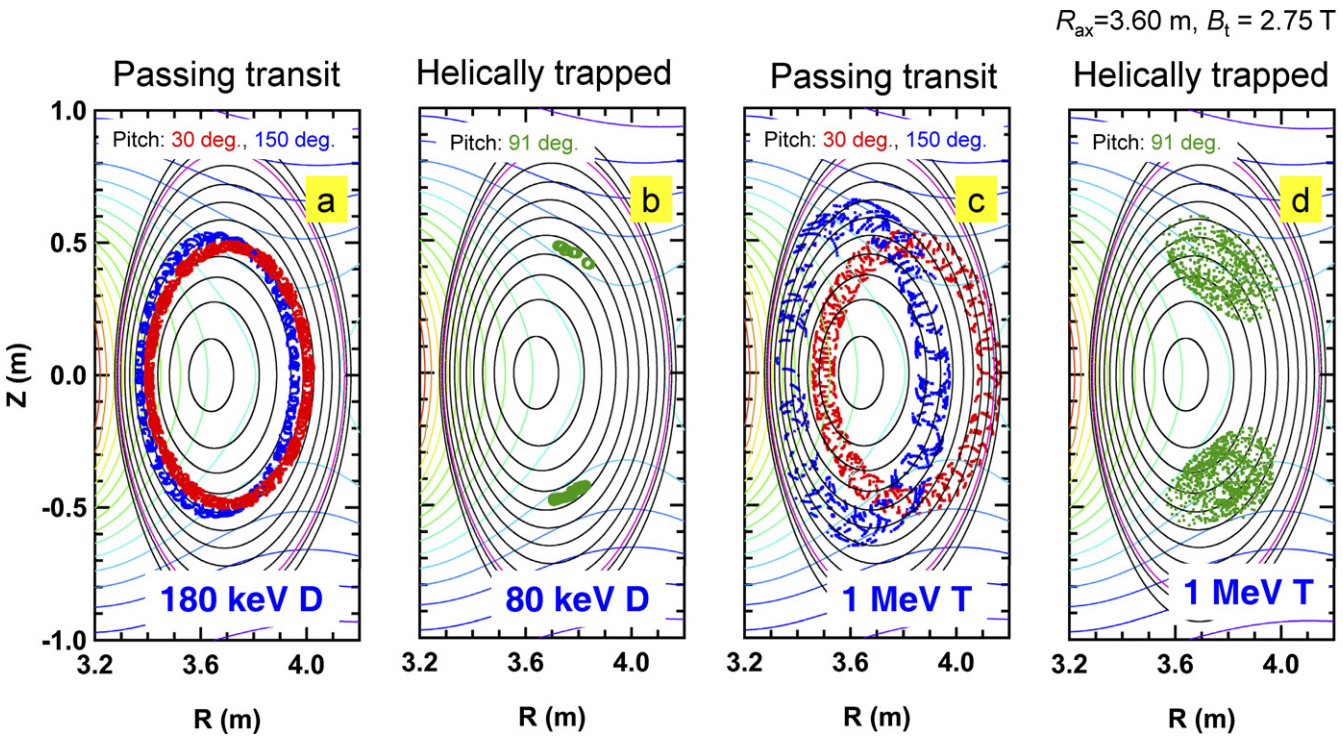

Figure 3. Typical Poincaré plot of beams (*a*), (*b*) and 1 MeV tritons (*c*), (*d*) calculated by Lorentz orbit code (LORBIT). The color contour shows the magnetic field strength and the black line shows the magnetic flux surface. The pink line shows the rotational transform of 1 surface where EIC excites.

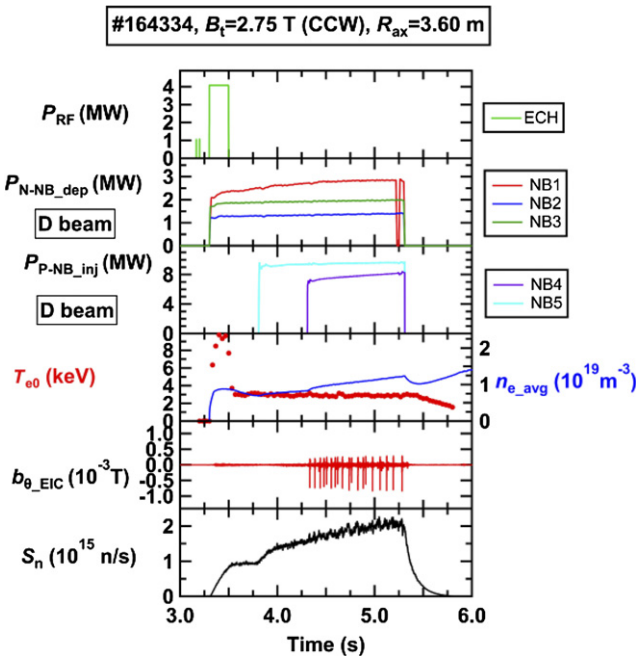

Figure 4. Typical waveform of an EIC discharge. N-NBs and P-NBs inject deuterium beams. S_n reflects the global confinement of passing transit beam ions injected by N-NBs and helically-trapped beam ions injected by P-NBs.

line-averaged electron density measured by a far infrared interferometer are 3 keV and 10^{19} m^{-3}, respectively. EIC having the magnetic fluctuation amplitude of 10^{-3} T was observed with a magnetic probe located on the vacuum vessel. The poloidal mode number/toroidal mode number of EIC are 1 and 1. The peak position of EIC is located on the normalized minor radius (r/a) of 0.85. The relative amplitude of EIC at the peak position (dB/B) is evaluated to be approximately 7×10^{-4} T [18, 36]. EIC bursts appeared from t of 4.3 s to 5.3 s, when all the NBs were injected. In particular, both P-NB injections are needed to excite EIC. The magnetic probe array shows that the EIC has a toroidal mode number of 1 and a poloidal mode number of 1. The EIC has a peak at the normalized minor radius of 0.9, where the rotational transform is of 1 (figure 3). A gradual increase of S_n was observed according to N-NB and P-NB injections. The small depressions of S_n were observed at the EIC timing. Figure 5(*a*) shows the enlarged figure of figure 4. In this phase, all the NBs were continuously injected. Due to EIC bursts, which occurred at t of 4.67 s and 4.74, S_n concurrently drops down by approximately 2×10^{14} n s^{-1} within less than 10 ms, which is 11% of S_n. At the bottom of figure 5(*a*), the components of S_n calculated by the CONV_FIT3D code [54] and TASK/FP code [55] are shown. Here, S_{n_NNB}, $S_{n\_NNB\_BB}$, S_{n_PNB} and S_{n_TH} represent S_n from N-NB ion and plasma reactions, S_n from N-NB ion and N-NB ion reactions, S_n from P-NB ion and plasma reactions, and S_n from thermal reactions, respectively. In CONV_FIT3D models, the slowing down of NB ions based on the classical confinement considering the confinement time of NB ions was calculated. The confinement time of NB ions is given based on the short-pulsed NB experiment [54]. Then, the neutron production rate due to beam deuteron and thermal deuteron is calculated using a fusion cross-section. Here, the effective ion charge (Z_{eff}) was set to be 3.2. The ratio of beam–beam

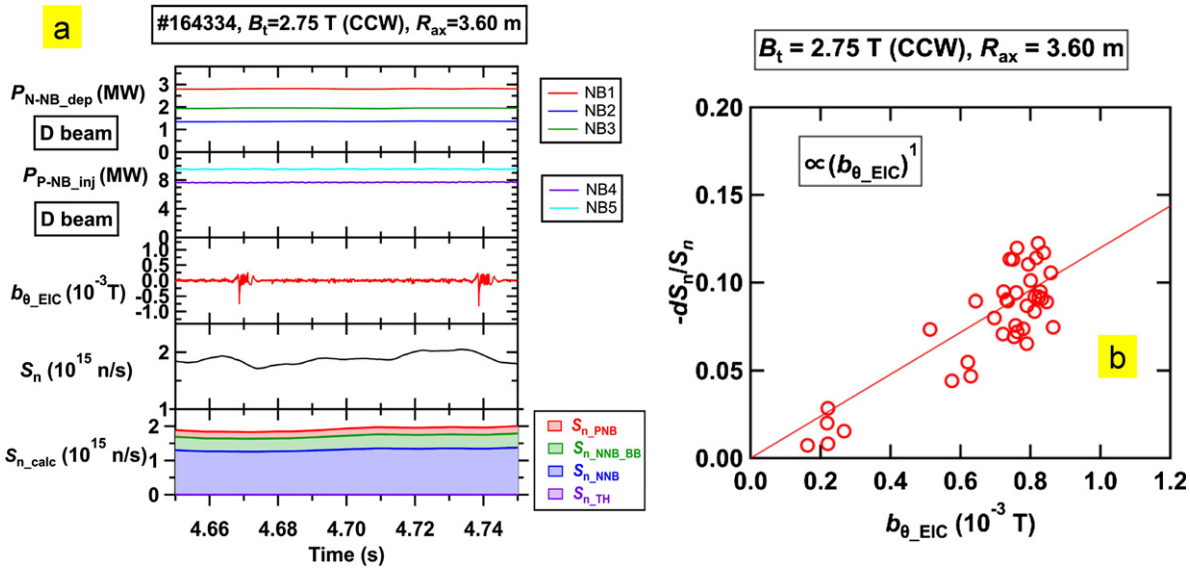

Figure 5. (*a*) Enlarged time evolution of an EIC discharge with the total neutron emission calculation by the CONV_FIT3D and TASK/FP codes. Due to EIC burst, S_n decreases by approximately 2×10^{14} n s^{-1}, which is 11% of S_n. (*b*) Dependence of drop rate of total neutron emission rate on EIC amplitude measure by a magnetic probe. Drop rate linearly increases and reaches ∼13%.

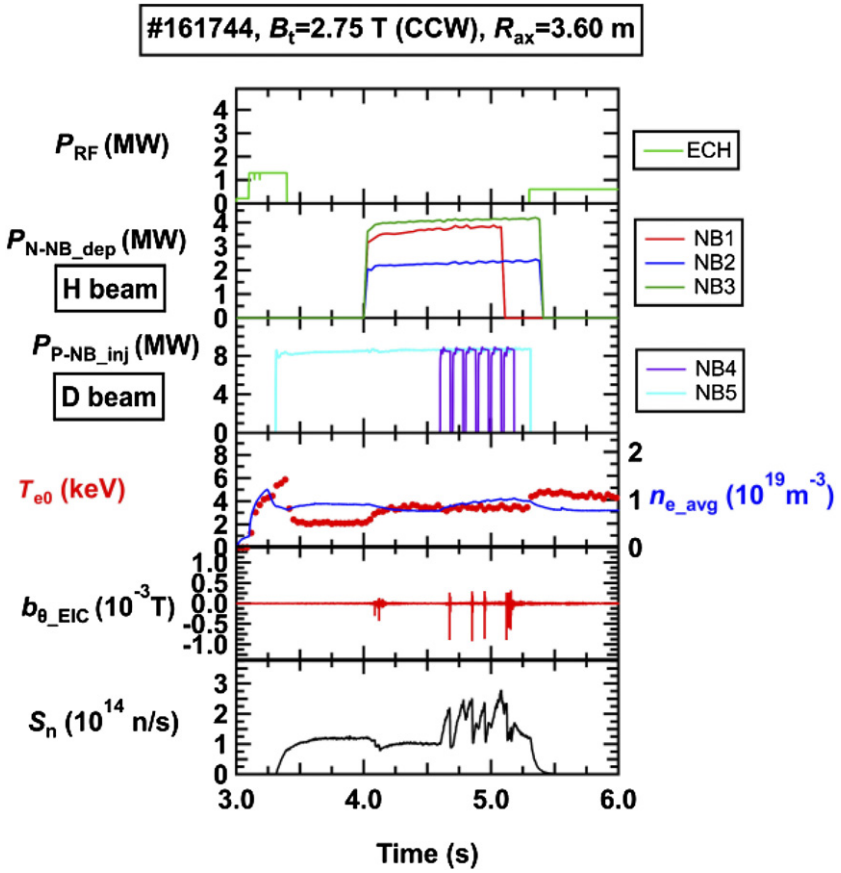

Figure 6. Typical waveform of an EIC discharge. N-NBs inject hydrogen beams and P-NBs inject deuterium beams. S_n reflects global confinement of helically-trapped beam ions injected by P-NBs.

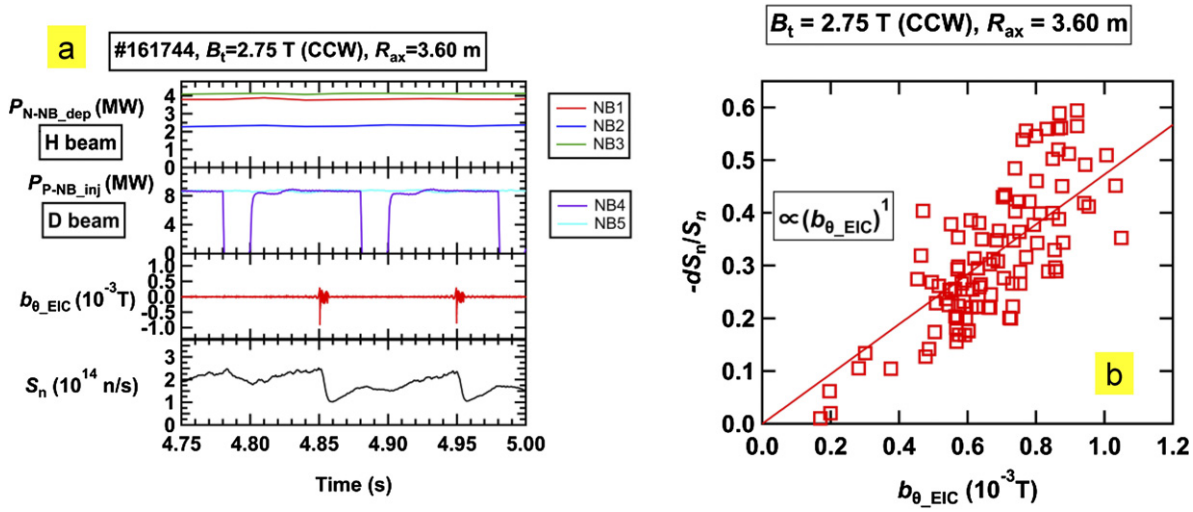

Figure 7. (*a*) Enlarged time evolution of EIC discharge with hydrogen N-NBs and deuterium P-NBs. Due to EIC burst, S_n decreases by approximately 1×10^{14} n s^{-1}, which is 55% of S_n. The decrement of S_n by EIC burst is almost half of the decrement of S_n in full deuterium beam cases. (*b*) Dependence of drop rate of total neutron emission rate on EIC amplitude measure by a magnetic probe. The drop rate of S_n increases linearly with EIC amplitude and reaches 60%.

neutron emission on S_{n_NNB} was evaluated using TASK/FP code, which calculates the neutron emission rate using a fusion cross-section based on the deuteron distribution in one dimension for real space and two dimensions for velocity space by the Fokker–Planck equation. In this analysis, a significant DD fusion neutron rate due to considerable relative velocity of beam ions fulfilled by opposite injection of NBs, e.g. N-NB1 (N-NB3) and N-NB2, is considered. The N-NB-ion-N-NB-ion fusion component is calculated to be approximately 30% of S_{n_NNB}. It is worth noting that the ratio of $S_{n\_NNB\_BB}$ on S_{n_NNB} is almost three times higher than the previous experiments [30] because the bulk deuteron density becomes almost a half in this experiment. It is found that in this discharge, S_{n_NNB}, $S_{n\_NNB\_BB}$, S_{n_PNB} and S_{n_TH} comprise ~10%, ~21%, ~69%, and ~0.2% of S_n, respectively. Figure 5(*b*) shows the drop rate of S_n as a function of the EIC amplitude measured by a magnetic probe. The dependence shows the energetic particle loss process [44]. The least-squares power fitting with no offset shows that the drop rate almost linearly increases with the EIC amplitude and reaches approximately 13% at EIC amplitude of 0.8×10^{-3} T. Here, the fitting curve is derived with least squares fitting. The linear relation shows that the dominant loss process is the convective type [17, 52]. The barely confined beam ions, which stayed near the confinement-loss boundary, were lost dominantly due to EIC. In this discharge, S_n reflects the global confinement of the N-NB and P-NB ions. Although the main driver of S_n was seen to be N-NB, to confirm that the drop in S_n is indeed due to the interaction between the EIC and N-NB, an additional study to isolate this effect is needed.

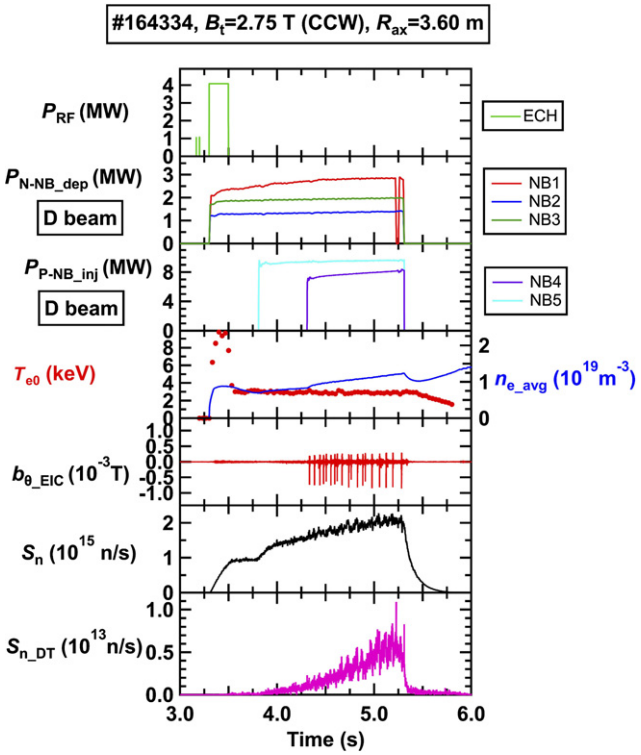

Figure 8. Typical waveform of an EIC discharge with deuterium N-NB and P-NB injections. Total DT neutron emission rate is measured by the middle Sci-Fi detector.

To determine the EIC effect on N-NB ions or P-NB ions separately, EIC discharges using hydrogen N-NBs and deuterium P-NBs were performed (figure 6). The central electron temperature and the line-averaged electron density are 3 keV and 10^{19} m^{-3}, respectively, which are almost the same parameters as the EIC experiment with full deuterium NBs. The total deposition power of the N-NBs reached 10 MW and the total injection power of the P-NBs reached 16 MW. The deposition power of the N-NB increased from full deuterium NB cases by 3 MW. Note that the modulation of NB4 was for the ion temperature measurement using a charge exchange recombination spectroscopy. Figure 7(*a*) shows the enlarged time

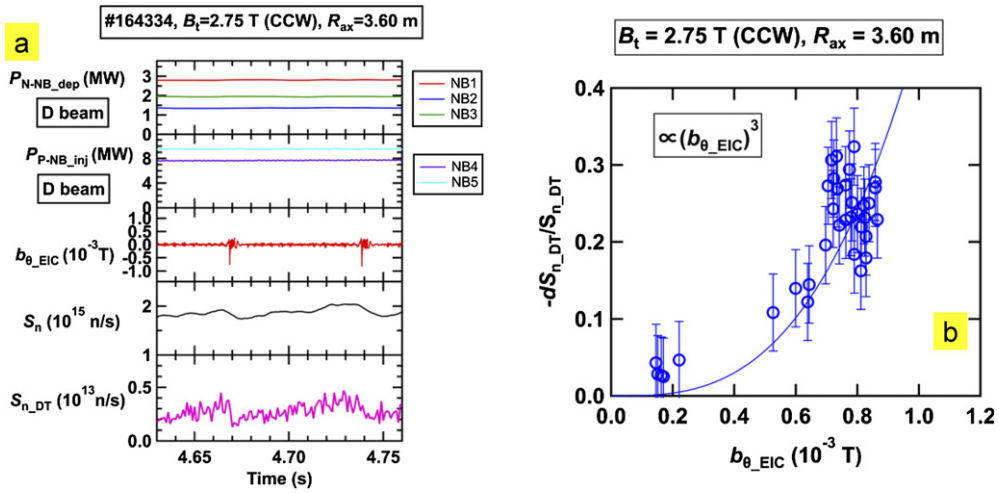

Figure 9. (*a*) Enlarged waveform of an EIC discharge with deuterium N-NB and P-NB injections. (*b*) Dependence of the drop rate of the total DT neutron emission rate on the EIC amplitude. The drop rate significantly increases with the EIC amplitude and reaches 30%.

evolution of figure 6. NB1, NB2, NB3, and NB5 were continuously injected in this phase. EIC bursts were observed when all the NBs were injected. Although the EIC amplitude is almost the same as the amplitude observed in the full deuterium NB case, S_n drops significantly compared with the full deuterium NB cases. The absolute value of the S_n decrease due to the EIC burst is significantly less compared with the S_n decrease in th full deuterium case approximately 1×10^{14} n s^{-1}, corresponding to 55% of S_n, which is almost the half of the S_n decrease in full deuterium NB cases. In this discharge, S_n reflected the global confinement of P-NB ions. The significant amount of the S_n decrease shows that the P-NB ion losses due to the EIC burst are substantial. Figure 7(*b*) shows the dependence of the drop rate of S_n as a function of the EIC amplitude. The least-squares power fitting with no offset shows that the drop rate of S_n increases almost linearly with EIC amplitude and reaches 60% at EIC amplitude of 0.9×10^{-3} T. The linear increase of the drop rate of S_n with EIC amplitude is consistent with the result obtained in the full deuterium NB cases. In the full deuterium NB case, the drop rate of S_n reached 13%. Therefore, it is found that in the full deuterium NB case the contribution of P-NB loss is approximately 6% because 10% of S_n is comprised of P-NB components from CONV_FIT3D and TASK/FP calculation. Then, the remainder of the 7% drop of S_n corresponds to the N-NB components. Therefore, EIC induces approximately 6% loss of N-NB ions because $S_{n\_NNB\_BB}$ and S_{n_NNB} compromise ∼21% and ∼69% of S_n, respectively, if N-NB1, N-NB2, N-NB3 ions are assumed to be lost equally. Hence, EIC induces up to a 6% loss of passing ions and up to a 60% loss of P-NB ions. Note that the reason for observing substantial transport of P-NB ions compared with N-NB ions is that EIC is excited by P-NB ions, because P-NB ions exchange energy and momentum more efficiently with the EIC mode.

3.2. 1 MeV triton transport due to EIC

In EIC discharges with a full deuterium beam condition, the time evolution of the secondary DT neutron rate was measured using the middle Sci-Fi detector (figure 8). Here, the time evolution of S_{n_DT} is plotted at the bottom of figure 8. In this magnetic configuration, triton confinement capability is relatively high because of the high B_t and inward shift of R_{ax} [26]. A gradual increase of S_{n_DT} is observed with the middle Sci-Fi detector. The relatively long rise time of S_{n_DT} rather than the rise time of S_n is due to the difference of cross-section curves between DD and DT fusion reactions. The cross-section of the DD reaction monotonically increases with the deuteron energy toward the injection energy of the beam, whereas the cross-section of the DT reaction has a peak at an energy of approximately 100 keV. Therefore, the cross-section of DT neutrons increases with the slowing down of triton energy from 1 MeV to 100 keV. Figure 9(*a*) shows the enlarged time evolution of figure 8. The absolute calibration of S_{n_DT} was performed using the neutron activation system with 10 pieces of silicon foils. The obtained calibration factor is 10^8 DT neutrons per pulse count. Time evolution shows that the decay time of S_{n_DT} due to EIC was ∼2 ms. S_{n_DT} drops rapidly compared with S_n due to EIC. The time evolution shows 1 MeV tritons escaped from the plasma immediately compared with beam ions. Figure 8(*b*) shows the drop rate of S_{n_DT} as a function of the EIC amplitude. The drop rate reaching ∼30% suggests that approximately 30% of fusion-born tritons are lost due to EIC. The least-squares power fitting with no offset shows that the drop rate of S_{n_DT} increases with EIC amplitude to the third power. The relatively high power shows that not only tritons confined in the confinement-loss boundary, but also the tritons confined near the core region, are transported substantially. As shown in figures 3(*c*) and (*d*), 1 MeV tritons are barely confined; therefore, tritons are easily transported due to MHD instabilities. In previous studies, the first power and second power correspond to the convective type and diffusive type loss. The third power shows the significant transport [52]. Unlike P-NB ions, the major component of a DD-born triton is thought to be away from the resonant condition because the initial velocity distribution of the tritons is isotropic, and the triton has a slowing down distribution consisting of broadband energy. The primary transport process of the tritons due

to EIC might be non-resonant. One of the possible reasons for the exponent higher than two might be due to the strong transport due to the non-resonant process. The other possibility is the effect of the radial electric field formed due to EIC. The previous measurement of the heavy-ion beam probe showed that plasma potential at the center drops up to 20 kV [42]. Also, the radial electric field largely changes. The significant and rapid potential change might enhance the transport of tritons having an energy of approximately 100 keV. The potential changes due to the EIC can be the reason for inducing significant transport. The detailed analysis of our understanding of the transport process of tritons due to EIC using numerical simulations such as GNET [56]/DELTA5D [57] plus MCNP6 models [58] or ASCOT [59] plus Serpent [60] models and comparison of the transport process of P-NB ions will form the basis for future work.

4. Summary

Energetic ion transport due to energetic-ion-driven MHD instability is studied using comprehensive neutron diagnostics in the LHD to contribute to our understanding of alpha particle confinement in a fusion burning plasma. Passing transit and helically-trapped beam ion transport due to EIC excited by helically-trapped beam ions is observed by S_n measurement using NFM. The drop rate of S_n due to EIC increases linearly with the EIC amplitude. The relation shows that the beam ions existing near the confined-loss boundary are mainly lost with the convective process. Additional experiments performed with hydrogen N-NBs and deuterium P-NBs indicate that EIC induces up to a 60% loss of helically-trapped beam ions and up to a 6% loss of transit beam ions, which is the main heating source of the LHD. A Sci-Fi detector with a relatively high sensitivity to DT neutrons is developed and utilized to perform a time-resolved triton confinement study with a relatively high temporal resolution. A substantial and rapid drop of DT neutron emission rate due to EIC is observed using the Sci-Fi detector. Drop of S_{n_DT} due to EIC increases with the EIC amplitude to the power of three. The relation shows that not only tritons confined in confined-loss boundary, but also tritons confined in the inner region of a plasma, are substantially transported due to EIC because 1 MeV tritons are barely confined due to the large Larmor radius. Knowledge of the energetic ion transport process due to energetic-ion-driven MHD instability using various spatial and velocity distributions will contribute to our understanding of alpha particle confinement in a future fusion reactor.

Acknowledgments

This work was supported by the NINS program of Promoting Research by Networking among Institutions (Grant No. 01411702), and by NIFS Collaboration Research programs (KOAH037). This work was also partly supported by JSPS KAKENHI Grant No. C19K03798 and the Japan-Korea Fusion Collaboration Program.

ORCID iDs

K. Ogawa https://orcid.org/0000-0003-4555-1837
M. Isobe https://orcid.org/0000-0002-3572-1882
H. Nuga https://orcid.org/0000-0003-3293-488X
S. Kamio https://orcid.org/0000-0003-0755-2433
Y. Fujiwara https://orcid.org/0000-0003-2985-060X
M.I. Kobayashi https://orcid.org/0000-0003-0920-2154
S. Sangaroon https://orcid.org/0000-0002-0160-0468
E. Takada https://orcid.org/0000-0002-4058-2661
R. Seki https://orcid.org/0000-0002-5364-805X
H. Yamaguchi https://orcid.org/0000-0002-1177-3370
S. Murakami https://orcid.org/0000-0002-2526-7137
M. Osakabe https://orcid.org/0000-0001-5220-947X

References

[1] Fasoli A. *et al* 2007 Progress in the ITER Physics Basis Chapter 5: Physics of energetic ions *Nucl. Fusion* **47** S264
[2] Zweben S.J. *et al* 1995 *Nucl. Fusion* **35** 893
[3] Sharapov S.E., Borba D., Fasoli A., Kerner W., Eriksson L.-G., Heeter R.F., Huysmans G.T.A. and Mantsinen M.J. 1999 *Nucl. Fusion* **39** 373
[4] Dumont R.J. *et al* 2018 *Nucl. Fusion* **58** 082005
[5] Heidbrink W.W. and Sadler G.J. 1994 *Nucl. Fusion* **34** 535
[6] Wolle B. 1999 *Phys. Rep.* **312** 1–86
[7] Heidbrink W.W. and Sager G. 1990 *Nucl. Fusion* **30** 1015
[8] Kass T., Bosch H.-S., Hoenen F., Lackner K., Maraschek M., Zohm H. and Team A.U. 1998 *Nucl. Fusion* **38** 807
[9] Ishikawa M. *et al* 2005 *Nucl. Fusion* **45** 1474
[10] von Goeler S., Roquemore A.L., Johnson L.C., Bitter M., Diesso M., Fredrickson E., Long D. and Strachan J. 1996 *Rev. Sci. Instrum.* **67** 473
[11] Duong H.H. and Heidbrink W.W. 1993 *Nucl. Fusion* **33** 211
[12] Marcus F.B. *et al* 1994 *Nucl. Fusion* **34** 687
[13] Nishitani T., Isobe M., Wurden G.A., Chrien R.E., Harano H., Tobita K. and Kusama Y. 1997 *Fusion Eng. Des.* **34–35** 563
[14] Osakabe M. *et al* 2010 *Fusion Sci. Technol.* **58** 131
[15] Osakabe M., Yamamoto S., Toi K., Takeiri Y., Sakakibara S., Nagaoka K., Tanaka K. and Narihara K. (LHD Experimental Group) 2006 *Nucl. Fusion* **46** S911
[16] Kamio S. *et al* 2020 *Nucl. Fusion* **60** 112002
[17] Ogawa K., Isobe M., Toi K., Watanabe F., Spong D.A., Shimizu A., Osakabe M., Ohdachi S. and Sakakibara S. 2010 *Nucl. Fusion* **50** 084005
[18] Ogawa K., Isobe M., Toi K., Spong D.A. and Osakabe M. 2012 *Nucl. Fusion* **52** 094013
[19] Toi K. *et al* 2004 *Plasma Phys. Control. Fusion* **46** S1
[20] Sigmar D.J. *et al* 1992 *Phys. Fluids* B **4** 1506
[21] Heidbrink W.W., Duong H.H., Manson J., Wilfrid E., Oberman C. and Strait E.J. 1993 *Phys. Fluids* B **5** 2176
[22] Ogawa K., Isobe M., Toi K., Shimizu A., Spong D.A., Osakabe M. and Yamamoto S. 2013 *Nucl. Fusion* **53** 053012
[23] Seki R., Todo Y., Suzuki Y., Spong D.A., Ogawa K., Isobe M. and Osakabe M. 2019 *Nucl. Fusion* **59** 096018
[24] Seki R. *et al* 2020 *J. Plasma Phys.* **86** 905860520
[25] Takeiri Y. 2018 *IEEE Trans. Plasma Sci.* **46** 2348
[26] Takeiri Y. *et al* 2018 *IEEE Trans. Plasma Sci.* **46** 1141
[27] Osakabe M. *et al* 2018 *Fusion Sci. Technol.* **72** 199
[28] Isobe M. *et al* 2018 *IEEE Trans. Plasma Sci.* **46** 2050
[29] Isobe M. *et al* 2018 *Nucl. Fusion* **58** 082004
[30] Ogawa K. *et al* 2019 *Nucl. Fusion* **59** 076017
[31] Ogawa K., Isobe M., Nishitani T. and Kobuchi T. 2018 *Rev. Sci. Instrum.* **89** 113509

[32] Ogawa K., Isobe M., Takada E., Uchida Y., Ochiai K., Tomita H., Uritani A., Kobuchi T. and Takeiri Y. 2014 *Rev. Sci. Instrum.* **85** 11E110
[33] Sangaroon S. *et al* 2020 *Rev. Sci. Instrum.* **91** 083505
[34] Ogawa K., Isobe M., Kawase H., Nishitani T., Seki R. and Osakabe M. 2018 *Nucl. Fusion* **58** 044001
[35] Ogawa K., Isobe M., Kawase H., Nishitani T., Seki R., Osakabe M. and Group L.E. 2018 *Plasma Phys. Control. Fusion* **60** 044005
[36] Ogawa K. *et al* 2020 *Nucl. Fusion* **60** 112011
[37] Ogawa K., Isobe M. and Osakabe M. 2021 *Plasma and Fusion Research* **16** 1102023
[38] Toi K., Ogawa K., Isobe M., Osakabe M., Spong D.A. and Todo Y. 2011 *Plasma Phys. Control. Fusion* **53** 024008
[39] Ido T. *et al* 2015 *Nucl. Fusion* **55** 083024
[40] Ido T. *et al* 2011 *Nucl. Fusion* **51** 073046
[41] Du X.D. *et al* 2015 *Phys. Rev. Lett.* **114** 155003
[42] Du X.D. *et al* 2015 *Nucl. Fusion* **56** 016002
[43] Isobe M. *et al* 2014 *Rev. Sci. Instrum.* **85** 11E114
[44] Ito D. *et al* 2021 *Plasma Fusion Res.* **16** 1405018
[45] Wurden G.A. *et al* 1995 *Rev. Sci. Instrum.* **66** 901
[46] Ogawa K., Isobe M., Nishitani T., Murakami S., Seki R., Nakata M., Takada E., Kawase H. and Pu N. 2018 *Nucl. Fusion* **58** 034002
[47] Takada E., Fujisaki A., Nakada N., Isobe M., Ogawa K., Nishitani T. and Tomita H. 2016 *Plasma Fusion Res.* **11** 2405020
[48] Takada E. *et al* 2019 *Rev. Sci. Instrum.* **90** 043503
[49] Ogawa K. *et al* 2021 *AAPPS Bull.* **31** 20
[50] Pu N. *et al* 2017 *Rev. Sci. Instrum.* **88** 113302
[51] Isobe M. *et al* 2009 *J. Plasma Fusion Res. Ser.* **8** 330 (http://www.jspf.or.jp/JPFRS/PDF/Vol8/jpfrs2009_08-0330.pdf)
[52] Miyamoto K. 2016 *Plasma Physics for Controlled Fusion* (Berlin: Springer) p 410
[53] Murakami S., Okamoto M., Nakajima N., Ohnishi M. and Okada H. 1994 *Nucl. Fusion* **34** 913
[54] Nuga H. *et al* 2020 *J. Plasma Phys.* **86** 81586030
[55] Nuga H., Seki R., Kamio S., Ogawa K., Isobe M., Osakabe M. and Yokoyama M. 2019 *Nucl. Fusion* **59** 016007
[56] Murakami S. *et al* 2006 *Nucl. Fusion* **46** S425
[57] Spong D.A. *et al* 2011 *Phys. Plasmas* **18** 056109
[58] Sugiyama S., Nishitani T., Matsuura H., Isobe M., Ogawa K., Tanaka T., Yoshihashi S., Uritani A. and Osakabe M. 2020 *Nucl. Fusion* **60** 076017
[59] Kontula J., Koschinsky J.P., Äkäslompolo S. and Kurki-Suonio T. 2021 *Plasma Phys. Control. Fusion* **63** 035022
[60] Äkäslompolo S. *et al* 2021 *Fusion Eng. Des.* **167** 112347